Electronic Supplementary Material (ESI) for Physical Chemistry Chemical Physics.
This journal is © the Owner Societies 2022

Electronic Supplementory Information

Chromone-methanol cluster in the electronic ground and lowest triplet state: A delicate interplay of non-covalent interactions

Pol Boden[a], Patrick H. Strebert[a], Marcel Meta[a], Fabian Dietrich[a,b], Christoph Riehn[a]*, Markus Gerhards†[a]

[a]Fachbereich Chemie & State Research Center OPTIMAS, TU Kaiserslautern, Erwin-Schrödinger-Str. 52, D-67663 Kaiserslautern, Germany.

[b]Núcleo Milenio MultiMat & Departamento de Ciencias Físicas, Universidad de La Frontera, Temuco, Chile.

Contents

Experimental results

R2PI experiments on chromone and chromone-methanol clusters

R2PI spectra were measured for chromone and the chromone-(MeOH)$_n$ clusters, based on previous experiments on chromone.[1] Since chromone as well as the structurally related xanthone[2] both undergo intersystem crossing (ISC) into the triplet manifold upon electronic excitation, an ISC is also expected for the chromone-(MeOH)$_n$ clusters. In the R2PI experiments, even at a delay of 23 µs between the excitation and ionization laser pulses, a strong ion signal was observed for the chromone-(MeOH)$_n$ aggregates, which makes an ISC plausible. For successful ionization, a two-color process was required with the excitation laser scanned between 32522 cm^{-1} and 34784 cm^{-1}. The frequency-fixed ionization laser was set to 46838 cm^{-1} and irradiated 70 ns after the excitation laser. For isolated chromone we reproduced the 0-0 transition at 33896 cm^{-1} (figure S1). Coordination of one or more methanol molecules leads to a red-shift, resulting in bands at 33292 cm^{-1} and 33204 cm^{-1} for the chromone-MeOH and chromone-(MeOH)$_2$ clusters, respectively. The band broadens significantly upon methanol coordination leading to unstructured spectra for the higher clusters, which are a first hint for UV fragmentation of larger clusters exhibiting similar UV absorption.

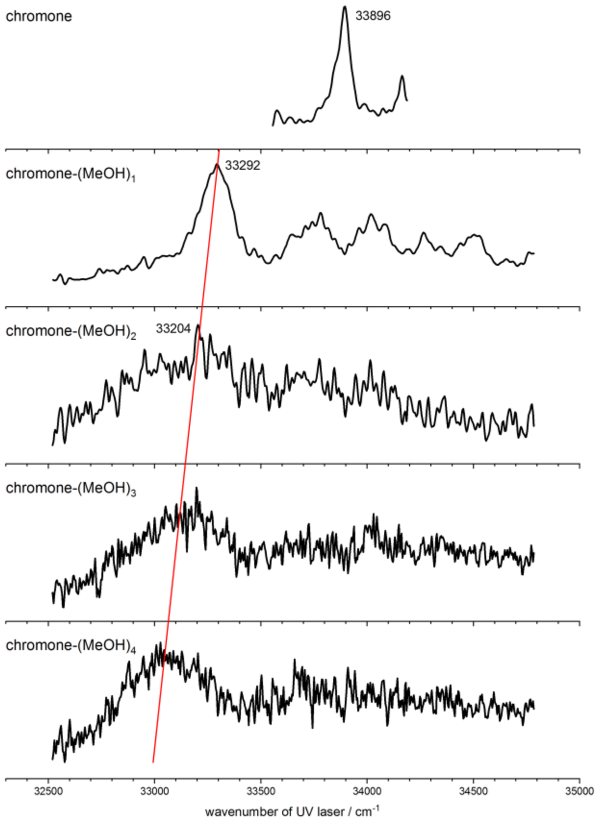

Figure S1: 2C-R2PI spectra for the mass traces of chromone and chromone-(MeOH)$_{1-4}$ (from top to bottom), with UV-ionization@46838 cm^{-1}. The redshift of the 0-0 transition upon addition of methanol is indicated with a red line as a guide to the eye.

Within the context of the expected intersystem crossing with the suspected subsequent "evaporative cooling" mentioned in the main manuscript, mass spectra with different time delays between the excitation and ionization laser pulses were recorded to analyze the cluster distribution over time. For the chromone monomer and the chromone-(MeOH)$_n$ clusters up to n=6, the integrated signal intensities were determined and illustrated in figure S2.

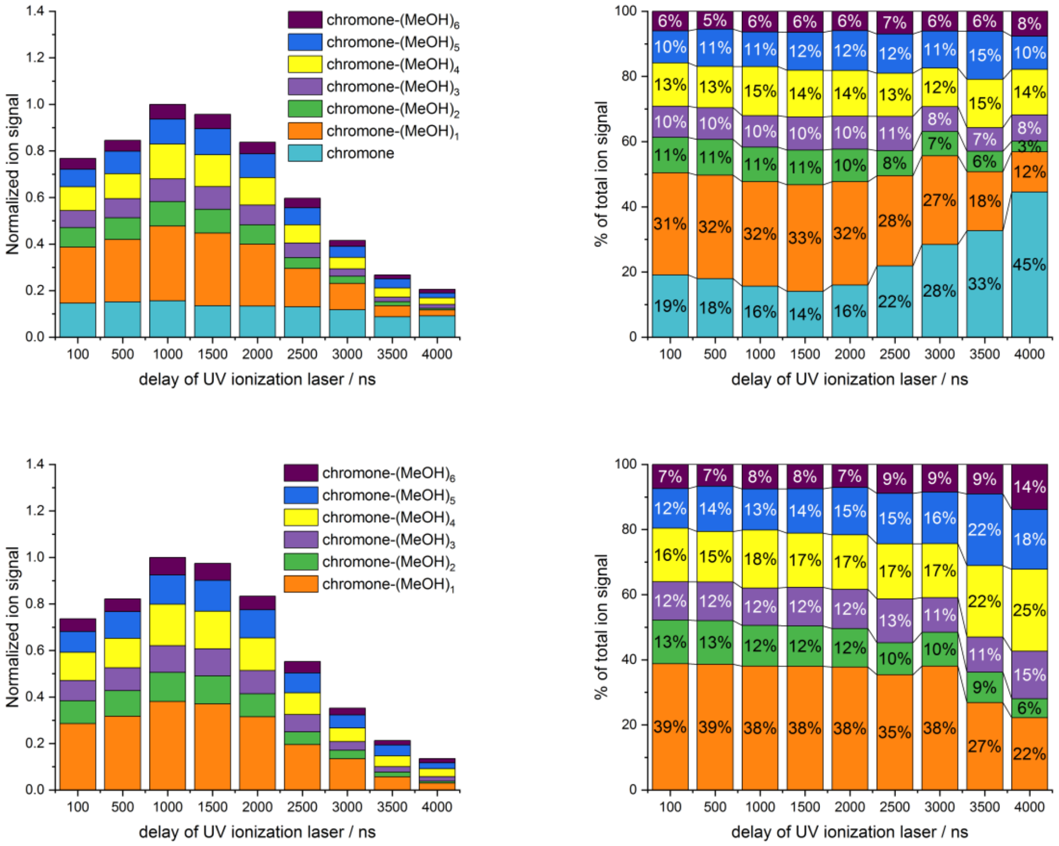

Figure S2: Normalized integrated ion signal intensities as a function of the time delay between the excitation and ionization laser pulses for chromone-$(MeOH)_n$ clusters (n=1-6) and the chromone monomer (top left, bottom left) and the same as relative proportions of the sum over all signals (top right, bottom right). Despite the significant time-dependence of the total ion signal, the cluster distribution does not change significantly for delays between 100 and 3000 ns, which is especially visible when excluding the chromone monomer mass trace (bottom right).

Focussing on the top left diagram, it is noticeable that the sum of all considered ion signals shows an increase from 100 to 1000 ns and a successive more pronounced decrease towards the final data point at 4000 ns. To determine the cluster distribution, the relative proportion of each species was calculated for each time delay, resulting in the plot at the top right. It can be seen, that only at larger delay times (> 2000 ns), the relative chromone monomer ion signal intensity increases at the cost of the chromone-$(MeOH)_{1,2}$ cluster signals, whereas the cluster distribution is constant for delays of 100 ns to 2000 ns.. Thus, the "evaporative cooling" process seems to be finished after at most 100 ns, since no significant changes in the cluster distribution can be observed afterwards until a delay of 2000 ns. This is also supported by the nearly constant absolute ion signal of the chromone monomer which should increase if fragmentation of chromone-$(MeOH)_n$ clusters occurs. It seems challenging to extract any further information from figure S2, as different effects could be responsible for the decrease of the chromone-$(MeOH)_n$ cluster signals at delays > 2000 ns. For instance, the excited state lifetime of the (potentially hot) clusters (partially originating from fragmentation of larger clusters) is unknown, but can be decisive for ionization *via* R2PI. Furthermore, the excitation and ionization laser beams have to be spatially separated with increasing time delay between excitation and ionization, so that the detection within the Time-of-flight mass spectrometer might also influence this behavior. Nevertheless, omitting the constant chromone monomer signal intensity from the calculation (bottom left, bottom right) reveals that the cluster distribution of the chromone-(MeOH)$_n$ clusters can even be considered “stable” until 3000 ns. This indicates that, most importantly, the cluster distribution does not show significant changes for a time frame of 100 ns to 3000 ns and supports our claim that the “evaporative cooling” proposed in the manuscript is already completed at a shorter time scale.

IR/UV experiments on chromone-methanol

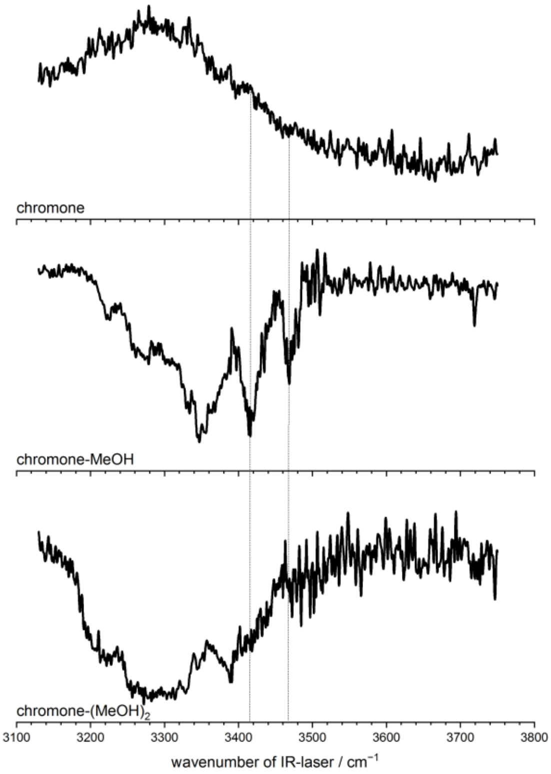

Figure S3: IR/R2PI spectra for the mass traces of chromone and chromone-(MeOH)$_{1\text{-}2}$, UV-excitation@33900 cm^{-1}, UV-ionization@46838 cm^{-1}; emphasizing that the features observed below 3400 cm^{-1} on the chromone-MeOH mass trace are due to laser-induced fragmentation from larger clusters.

Analyzing the IR/R2PI spectrum displayed in figure S3, the increase of the signal intensity on the chromone monomer trace can be attributed to IR fragmentation of chromone-solvent clusters. The features below 3400 cm^{-1} on the chromone-methanol mass trace are due to fragmentation effects of larger chromone-methanol clusters. Hereby, UV fragmentation effects should dominate, while the influence of (possibly weaker) IR fragmentation effects cannot be excluded. However, the two intense bands standing out at 3419 cm^{-1} and at 3470 cm^{-1} (highlighted with dashed lines) on the chromone-MeOH trace are unambiguously assigned to the chromone-MeOH species, as the other mass traces show no significant features in that spectral region (above 3400 cm^{-1}). The small peak at about 3720 cm^{-1} is a sign of fragmentation effects of larger chromone-(MeOH)$_n$-H_2O aggregates. The broad unstructured feature on the chromone-(MeOH)$_2$ trace is again very likely affected by UV (and possibly IR) fragmentation of larger and less stable clusters.

The UV/IR/UV spectrum (figure S4) shows a broad structured band on the chromone-MeOH mass trace (dashed line), which is definitely blue-shifted relative to the broad dip on the chromone-(MeOH)$_2$ trace. Thus, the major features on the chromone-MeOH trace can definitely be assigned to the chromone-MeOH species and are not due to fragmentation. The small peak at about 3720 cm^{-1} on the chromone-MeOH trace is explained by UV fragmentation of larger chromone-(MeOH)$_n$-H_2O

aggregates. The increase of the signal intensity on the chromone monomer trace is due to IR fragmentation of the chromone-MeOH species (and larger chromone-solvent clusters).

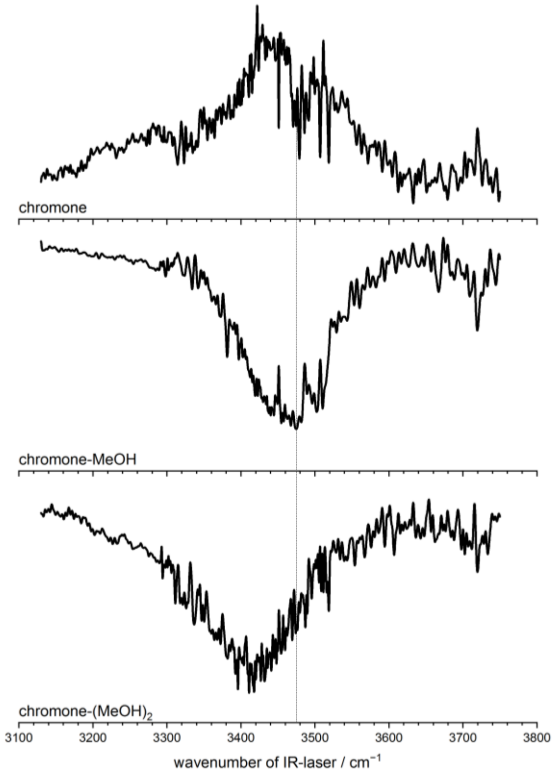

Figure S4: UV/IR/UV spectra for the mass traces of chromone and chromone-(MeOH)$_{1-2}$, UV-excitation@33900 cm^{-1}, UV-ionization@46838 cm^{-1}.

The sharp spikes which appear in the UV/IR/UV spectrum of chromone-methanol, in the spectral between 3450 and 3510 cm^{-1}, are caused by dips in the available IR laser power. For demonstration, the IR laser power curve for that spectral region is depicted in figure S5, together with the UV/IR/UV spectrum measured for chromone-methanol.

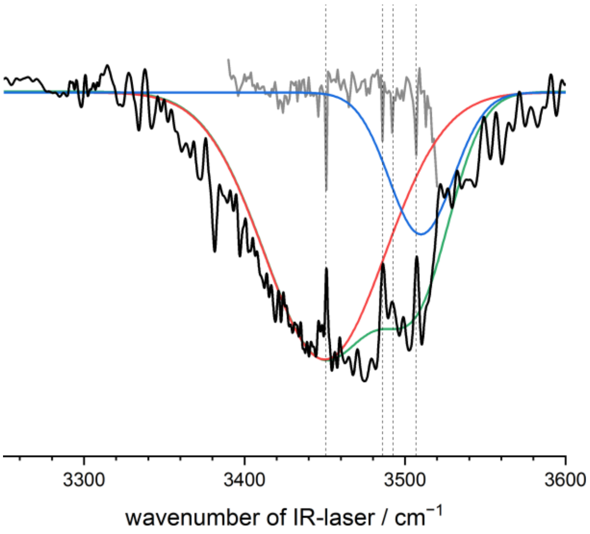

Figure S5: Laser power curve (grey trace) in comparison with the UV/IR/UV spectrum measured on the chromone-methanol trace. The correlation between the dips in the IR laser power curve and the discussed spikes observed in the IR experiment is illustrated by dashed grey lines.

Regarding the IR/R2PI and UV/IR/UV spectra of chromone-methanol a deconvolution with gaussians was performed (figure S6) to obtain a rough estimate for the relative population of the two competing isomers in the S_0 and T_1 state. For the S_0 state the ratio of both peak integrals amounts to 72:28 in favor of the outside isomer. Correcting for the different IR intensity of the bands results in a ratio of 66:34. Similarly, for the T_1 state, a ratio of 78:22 (uncorrected) and 72:28 (corrected) is obtained. Importantly, these values should only be understood as a rough estimate since other relevant factors as R2PI cross-sections, cooling efficiency and depletion efficiency cannot be addressed. Nevertheless, we can expect the increase in outside population to roughly match the increase in *ΔE* for the triplet state, which can be calculated by applying the Boltzmann formula, under the daring assumption that the temperatures in the S_0 and T_1 state are comparable. The preference for the outside isomer is clearly visible in the presented data, as well as the further increased population of the outside isomer in the excited state (see below). Interpretation of this value is difficult due to the inherent experimental errors. Nevertheless, the experimental prediction is close to the DLPNO-CCSD(T) value of 0.636, but differing significantly from the DFT value of 0.382 (DFT).

$$\frac{N(out)}{N(in)} = \exp(-\Delta E/RT)$$

$$\ln\left(\frac{N(out)}{N(in)}\right) = -\Delta E/RT$$

$$\frac{ln\left(\frac{N(out,S_0)}{N(in,S_0)}\right)}{ln\left(\frac{N(out,T_1)}{N(in,T_1)}\right)} = \frac{-\Delta E(S_0)/RT}{-\Delta E(T_1)/RT} = \frac{\Delta E(S_0)}{\Delta E(T_1)} = 0.702$$

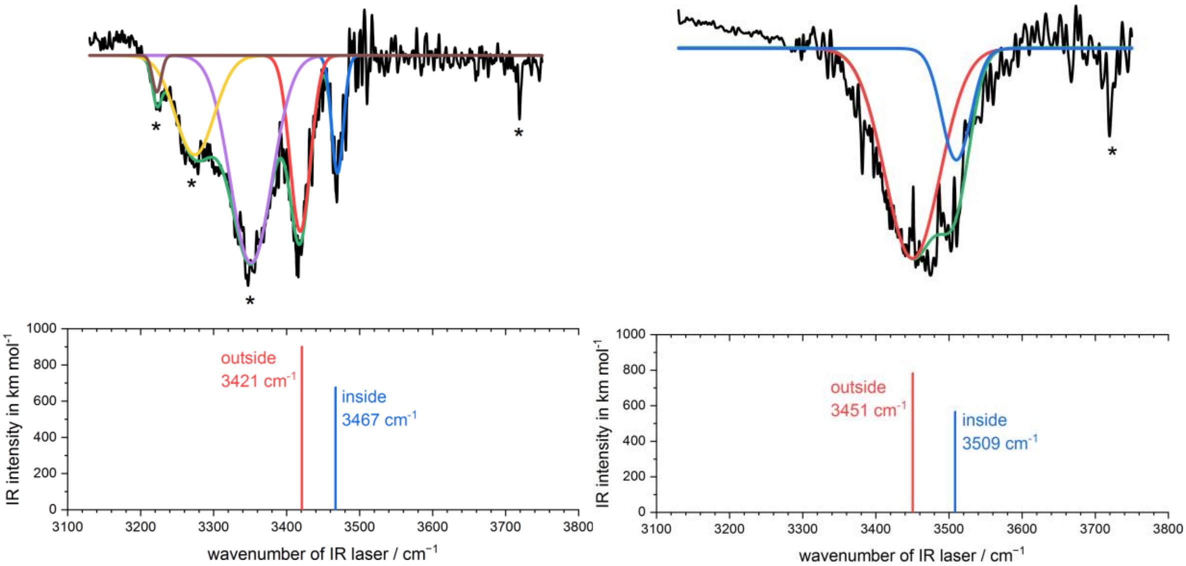

Figure S6: Theoretical and experimental IR spectra for the S_0 (left) and T_1 (right) state including gaussian fit functions to evaluate relative isomer populations. The convolution of all peaks (green) is composed of the inside (blue) and outside (red) peak with additional fragmentation peaks (purple, yellow, brown). Calculated OH stretching frequencies are obtained at CAM-B3LYP-D3(BJ)/def2-TZVP level, scaled by 0.95.

In the main manuscript, the experimental IR/R2PI were compared with the three energetically lowest structures since already the ether-bound cluster is energetically strongly disfavored compared to the carbonyl-bound clusters. Here, a full comparison of the experimental spectrum with all nine calculated isomers is shown (figure S7). All energetically less favored structures ($\Delta E > 15$ kJ mol^{-1}) show a strongly blue-shifted OH stretching vibration relative to the experiment. Furthermore, the IR intensity of the considered vibration is significantly lowered because no coordination with the highly polar carbonyl group takes place. Thus, only the first two isomers are taken into consideration.

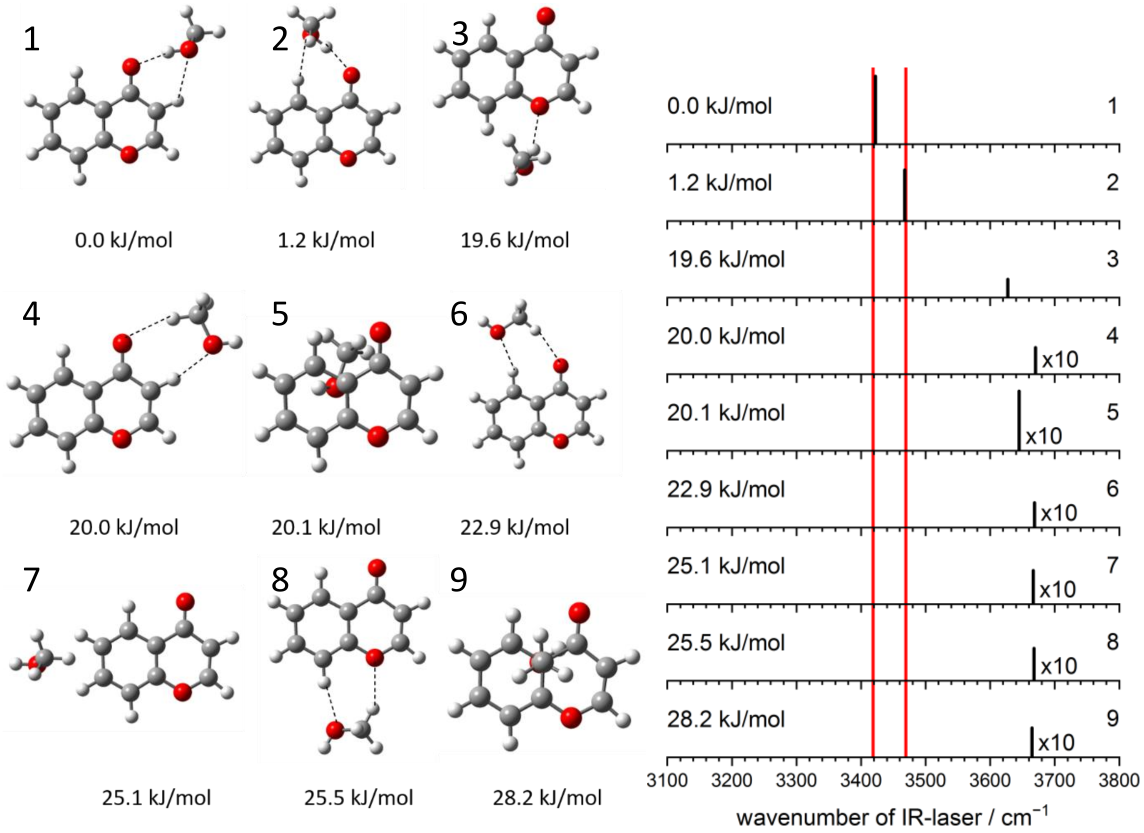

Figure S7: Calculated structures of chromone-MeOH with their respective electronic energies (left) and their respective IR spectra (right), compared with the experiment (red lines), showing that the carbonyl-bound structures exhibit the observed red-shift of the OH stretching band. Geometry optimizations and harmonic frequency calculations were performed at CAM-B3LYP-D3(BJ)/def2-TZVP level. Vibrational frequencies are scaled by 0.95.

IR/R2PI experiments on higher clusters

We also investigated the chromone-$(MeOH)_2$ complex in the electronic ground state, with the quantum chemical calculations identifying multiple structure types. For all energetically relevant isomers, a first methanol molecule is linked to the carbonyl group of the chromone unit. The additional methanol molecule is either hydrogen-bonded to the first solvent molecule (isomers 1-10 in figure S9) or can occupy another free binding site of chromone, such as the second free electron pair at the carbonyl oxygen atom (isomers 11-12 in figure S9). Hereby, the calculations clearly show that the first option is energetically advantaged, with a strong preference for the outside binding motif in comparison to the inside type. However, the measured spectrum (in figure S8) is not well resolved, so that we are not able to assign one specific structure to the experiment. Nevertheless, the outside-bound isomers 1 and 2, which are further stabilized *via* C–H···O contacts between chromone and the additional methanol molecule, exhibit the right pattern to be correlated to the spectrum, while (minor) contributions of other isomers, especially isomers 3-5 with occupation of the inside pocket, cannot be excluded. Finally, we cannot assign a specific outside-bound cluster, but may state that this motif contributes strongly to the experimental spectrum. This is further supported by the relative energy, which assigns the global minimum to these structures.

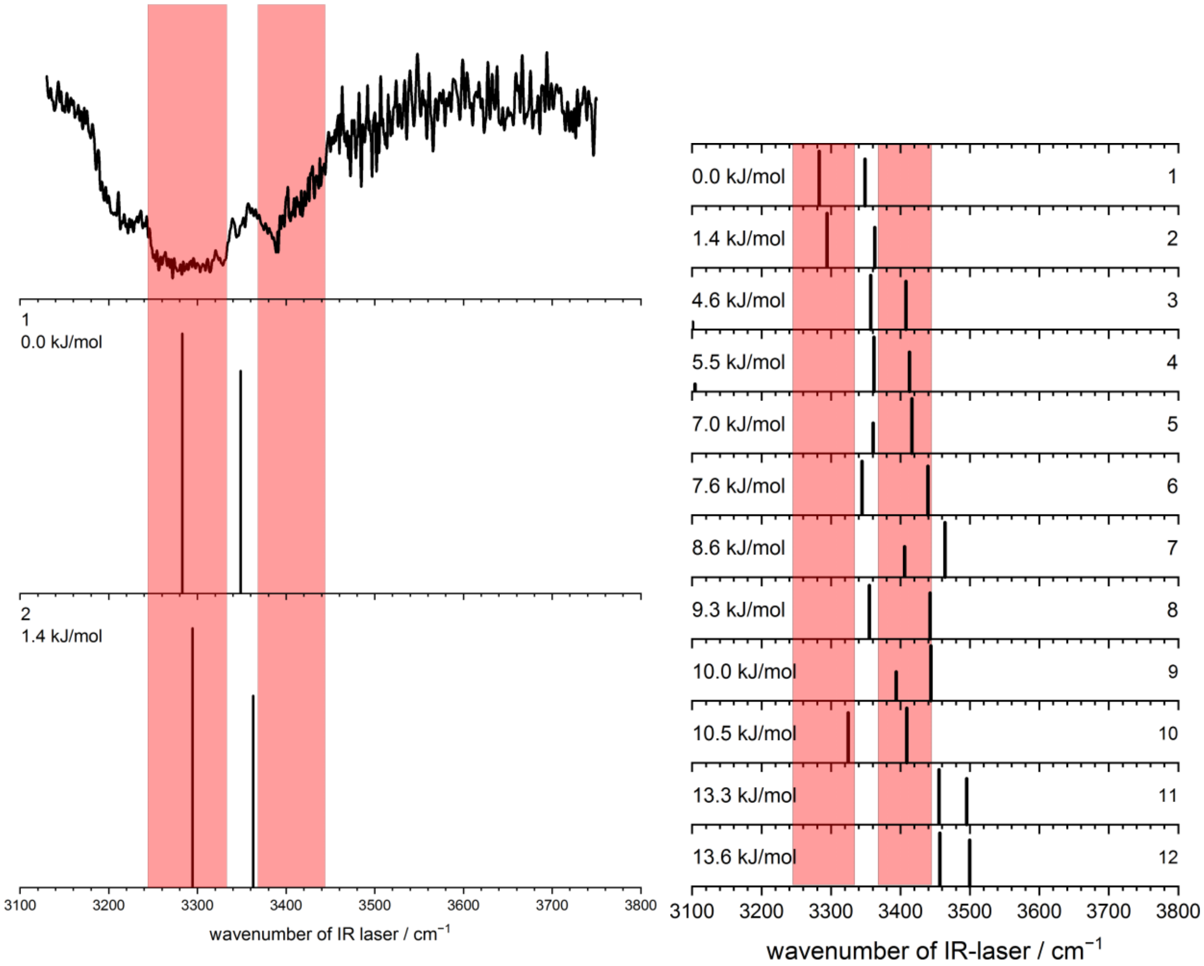

Figure S8: IR/R2PI spectrum of chromone-$(MeOH)_2$ compared with two calculated spectra of outside-bound clusters (left). A comparison with the IR spectra of all calculated structures is shown on the right, the red areas representing the broad features between 3244/3332 cm^{-1} and 3368/3445 cm^{-1}. The given energies refer to electronic energies. The two outside-bound structures may correlate with the observed experimental pattern, especially the most red-shifted band, although contributions of other isomers cannot be excluded. Geometry optimizations and harmonic frequency calculations were performed at CAM-B3LYP-D3(BJ)/def2-TZVP level. Vibrational frequencies are scaled by 0.95.

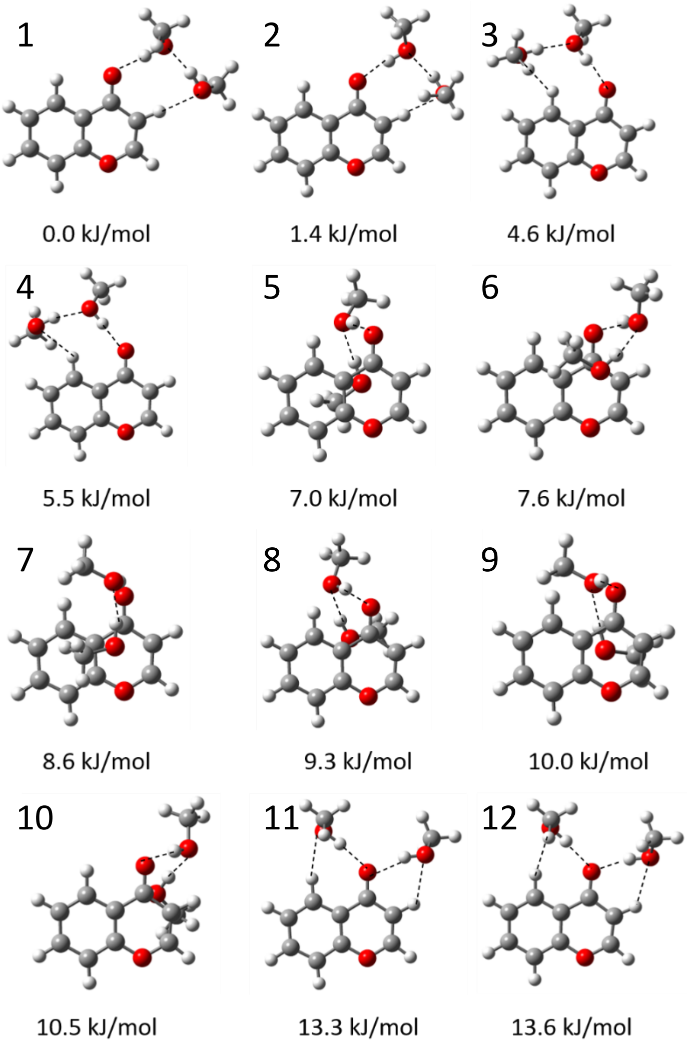

Figure S9: Optimized structures for the chromone-$(MeOH)_2$ cluster in the S_0 state with their respective electronic energies, as obtained at the CAM-B3LYP-D3(BJ)/def2-TZVP level.

Theoretical results

Further analysis of the excited states for chromone-methanol

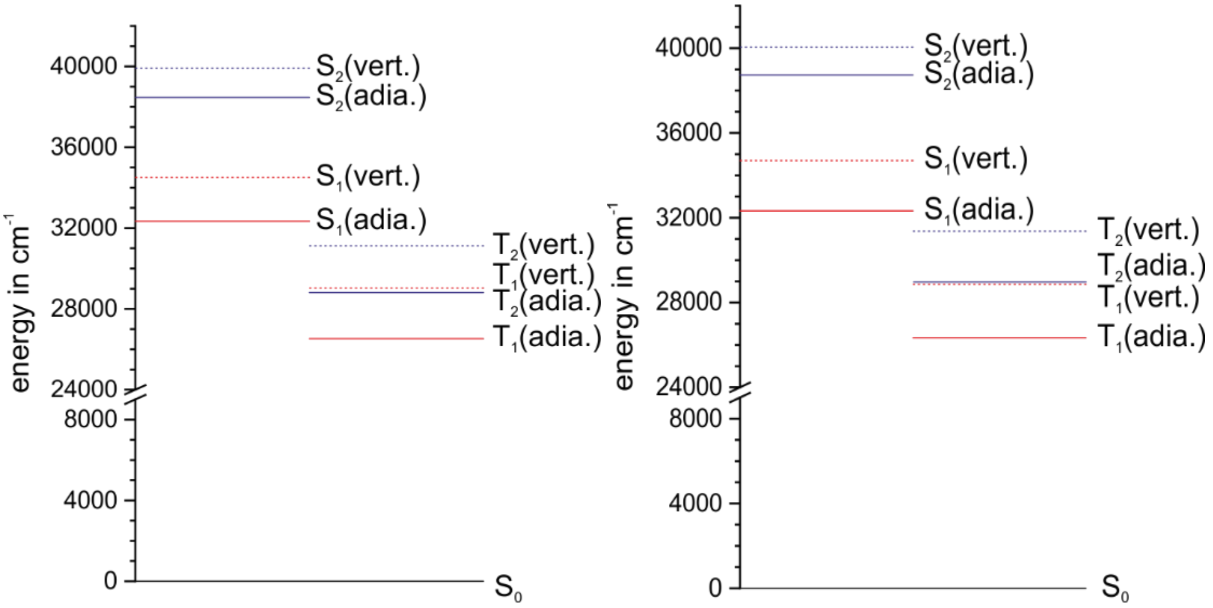

Figure S10: Jablonski diagram showing the first two singlet and triplet states, calculated at the TDDFT/CAM-B3LYP-D3(BJ)/def2-TZVP level; inside binding motif (left) and outside binding motif (right).

To analyze the electronic excitation and subsequent intersystem crossing, we calculated the excitation energies (figure S10) and natural transition orbitals (figures S11-S14) for the inside and outside isomers, for the first two excited singlet and triplet states using TDA-TDDFT/CAM-B3LYP/def2-TZVP. The usage of the Tamm-Dancoff approximation instead of the Random-Phase approximation was necessary to converge the calculations for the triplet states, while CAM-B3LYP was required to converge the excited singlet states. We observe a significant deviation from the experimental values since the band at 33292 cm^{-1} is assigned to the S_2 state, which is calculated at 39916 cm^{-1} (inside) and 40043 cm^{-1} (outside), respectively. Considering the character of the vertical excitations within the singlet manifold, we can state that the $S_0 \rightarrow S_1$ transition is of n, π^* type, while the $S_0 \rightarrow S_2$ transition is of π, π^* type. The calculations confirm the weakness of the $S_0 \rightarrow S_1$ transition, with a oscillator strength, which is weaker by a factor of around 8000 in comparison to the $S_0 \rightarrow S_2$ transition. The $S_0 \rightarrow S_2$ transition is of similar strength for the inside and outside motif. This should result in a negligible influence on the R2PI cross section, as mentioned in the main manuscript. Natural transition orbitals (NTO)[3] were calculated and are shown below (figures S11-S14). For the triplet manifold the $S_0 \rightarrow T_1$ transition is of π,π^* type while the $S_0 \rightarrow T_2$ transition is of n,π^* type. Interestingly, the T_2 and S_2 state are of different character, which could serve as an explanation for the observed strong intersystem crossing according to the rule of El-Sayed[4], leading to the assignment of an $S_2(\pi,\pi^*) \rightarrow T_2(n,\pi^*)$ intersystem crossing with subsequent internal conversion into the T_1 state, contradicting the assignment of the $^3(n,\pi^*)$ state as the lowest triplet state.[1] The energetic difference between the unrelaxed S_2 state and relaxed T_1 state amounts to 13387 cm^{-1} or 160 kJ mol^{-1} (inside) and 13709 cm^{-1} or 164 kJ mol^{-1} (outside), respectively. At this point it should also be noted that the T_1 state is definitely reached in the performed experiment, since the vibrational frequencies predicted for the chromone-methanol cluster in its T_2 state [3625 cm^{-1} (inside), 3651 cm^{-1} (outside), 3612 cm^{-1} (ether)] do not correlate with the measured UV/IR/UV spectrum.

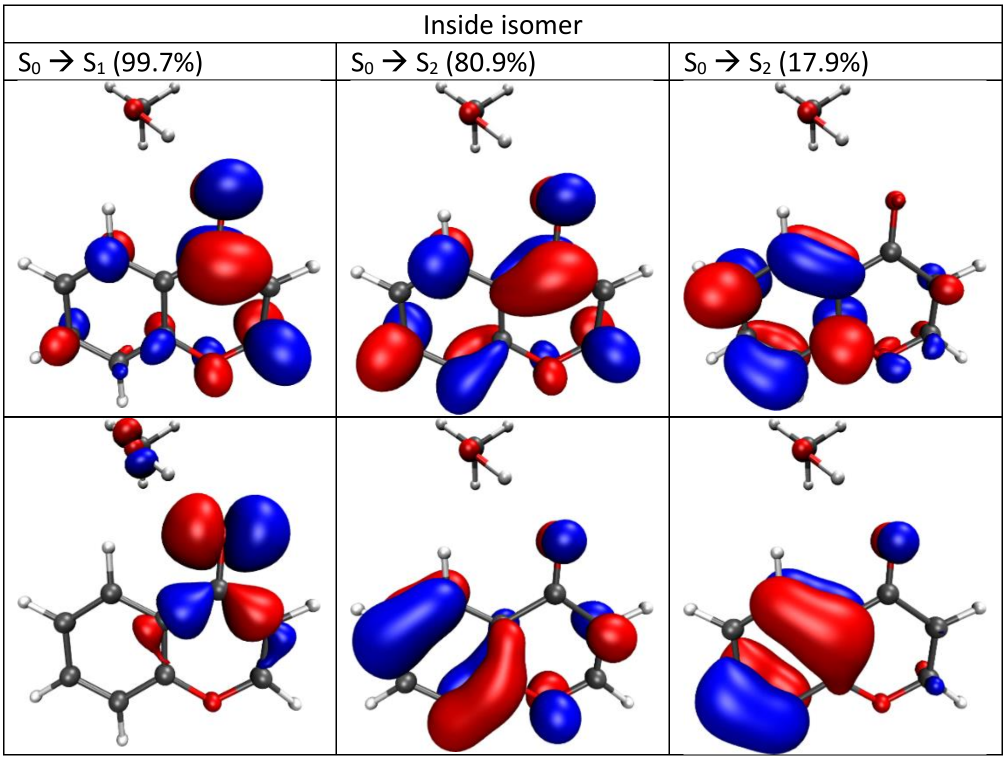

Figure S11: Natural transition orbitals, with occupied (bottom) and virtual (top) orbitals.

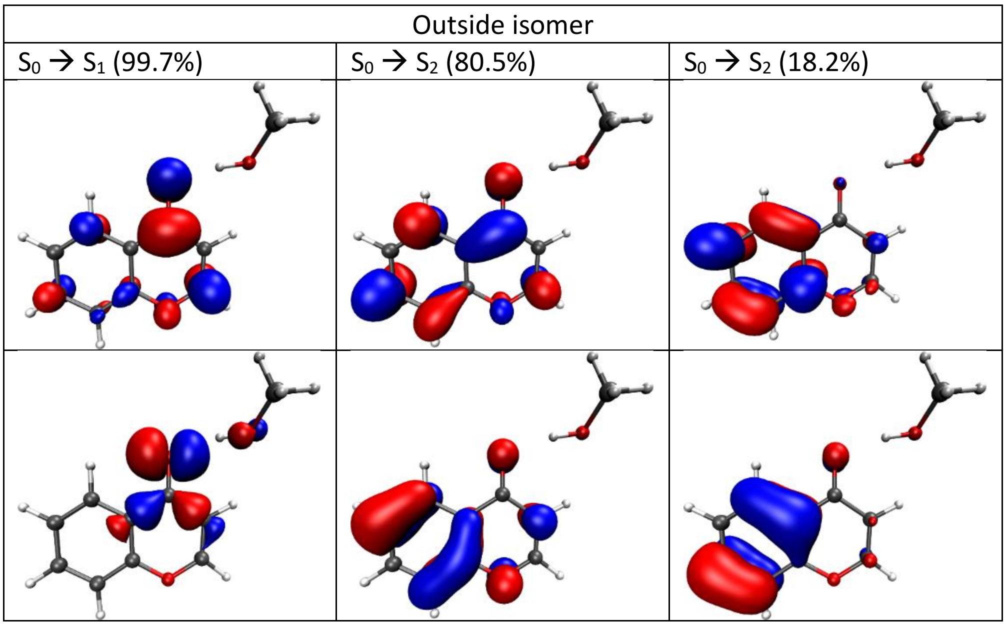

Figure S12: Natural transition orbitals, with occupied (bottom) and virtual (top) orbitals.

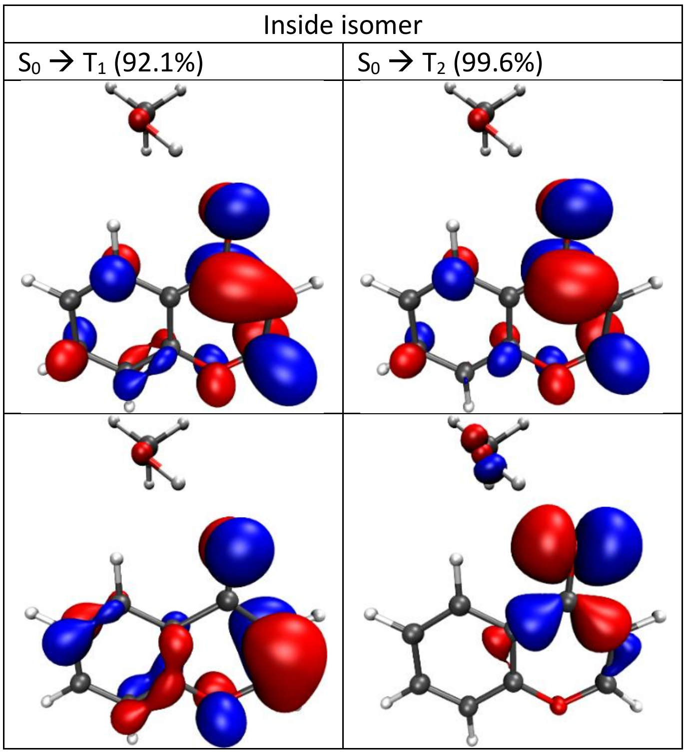

Figure S13: Natural transition orbitals, occupied (bottom) and virtual (top) orbitals.

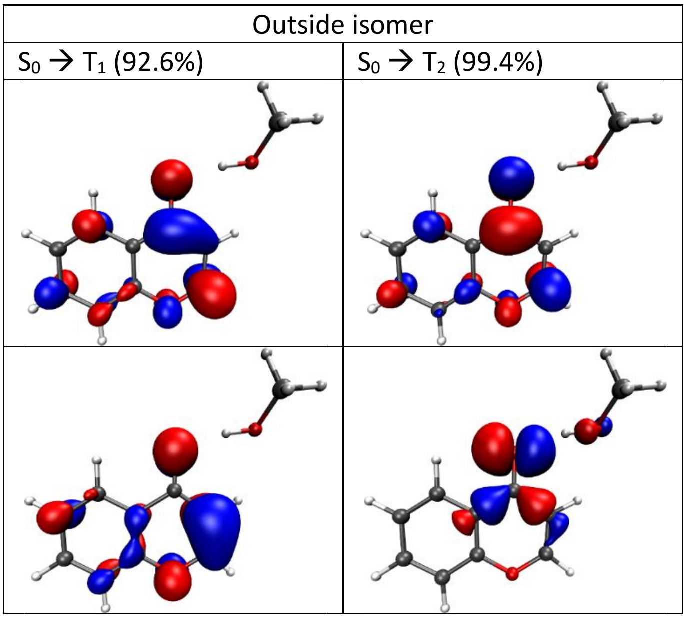

Figure S14: Natural transition orbitals, with occupied (bottom) and virtual (top) orbitals.

In the main manuscript, we refer to the triplet geometries calculated *via* UDFT not TDA-TDDFT, thus we performed TD-DFT calculations utilizing UDFT geometries to confirm that the order of the two triplet states is the same, which is indeed the case. The UDFT calculations allow us to handily extract the spin densities, which are plotted below (figure S15). The spin density is strongly localized on the distorted 4-pyrone ring of the chromone moiety, especially on the carbon atom next to the ether oxygen.

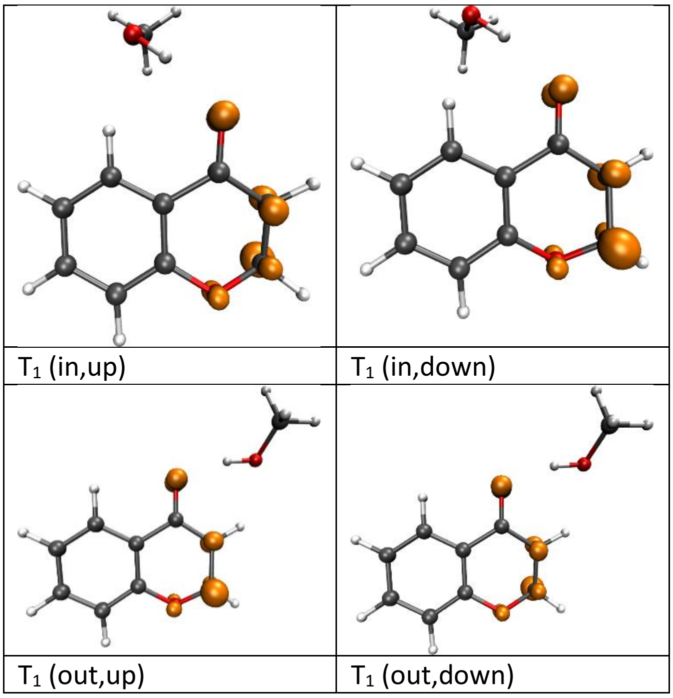

T_1 (in,up)

T_1 (in,down)

T_1 (out,up)

T_1 (out,down)

Figure S15: Spin densities of chromone-MeOH in the T_1 state, which are localized onto the 4-pyrone ring of the chromone molecule.

Further analysis of the T_1 state

The description of the lowest triplet state (T_1) is possible by either TD-DFT, using the S_0 as reference or UDFT, using the triplet state as reference. Both methods result in the loss of planarity of the 4-pyrone ring (see figure S16), resulting in “up” and “down” isomers for the triplet state. “Up” is referring to the geometry where the puckered carbon atom is on the same side of the 4-pyrone plane as the solvent molecule, “down” for the inverse configuration. Comparing the geometries calculated by TD-DFT (in red) and UDFT (in blue), the geometric distortion is much more pronounced for the latter (see figure S17). Both methods have in common that the geometric distortion is completely localized onto the 4-pyrone ring, which is demonstrated in figure S17, where all eight possible structures are displayed (UDFT/TD-DFT, in/out, up/down).

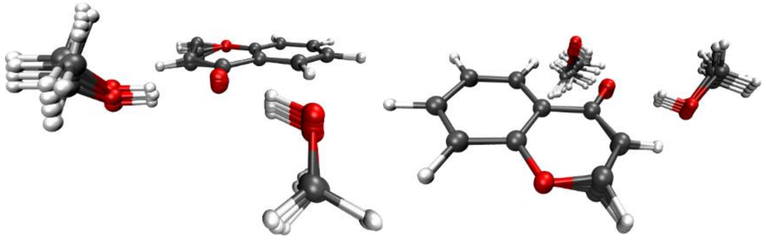

Figure S16: Overlay of all triplet structures, showing the conservation of the benzene ring planarity in chromone

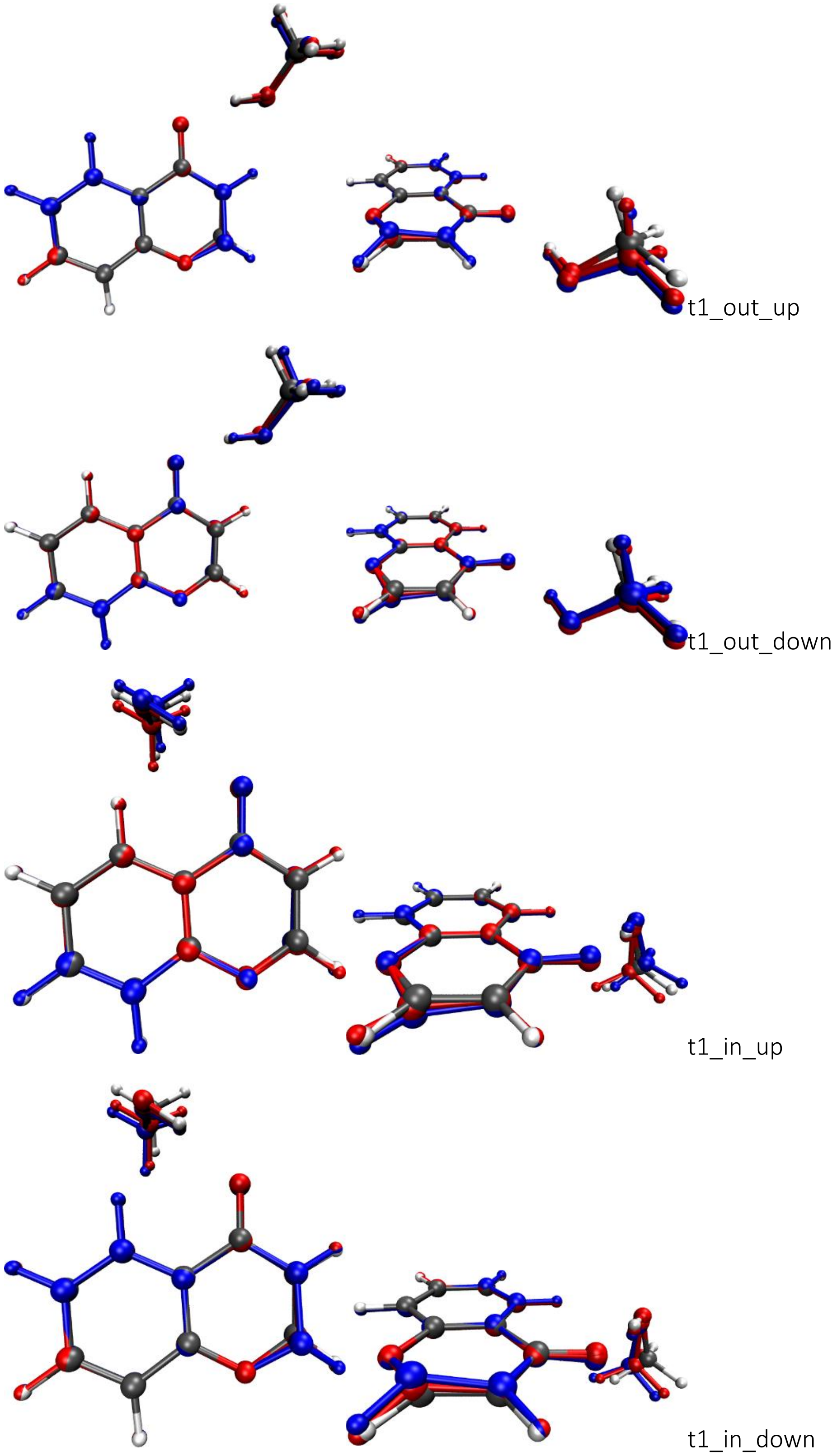

Figure S17: Overlay of multiple structures of chromone-MeOH, ground state (standard colors), TDDFT (red) and UDFT (blue), indicating that ring puckering is stronger in the UDFT case. From top to bottom: outside, up / outside,down / inside,up / inside,down. The stronger distortion of the 4-pyrone ring for the UDFT geometries is clearly visible as well as the conservation of the still planar aromatic ring.

To compare the quality of both approaches, SAPT0/jun-cc-pVTZ and DLPNO-CCSD(T)/def2-TZVP calculations were performed on the relaxed geometries, with the results shown in table S1.

Table S1: Comparison of electronic energies calculated with SAPT0/def2-TZVP and DLPNO-CCSD(T)/def2-TZVP for UDFT and TD-DFT inside/outside geometries in their respective up/down configuration, indicating that UDFT provides a better description of the system since TD-DFT geometries provide worse results (higher energy or failing) in most cases. The relative energies are in reference to the lowest energy of the outside,down structure obtained by UDFT.

Geometry	in	in	out	out	in	in	out	out
Puckering	up	down	up	down	up	down	up	down
Method	UDFT	UDFT	UDFT	UDFT	TD-DFT	TD-DFT	TD-DFT	TD-DFT
E(SAPT0) in kJ/mol	**-21.84**	**-21.82**	**-24.15**	**-24.25**	**n. a.**	**117.97**	**-27.86**	**-27.85**
ΔE(DLPNO-CCSD(T)) in kJ/mol	**2.69**	**2.39**	**0.07**	**0.00**	**7.73**	**7.30**	**5.53**	**5.63**

The data show that the UDFT geometries are able to describe both up and down isomers for the inside and outside structures in a satisfactory manner. The relative energies for the outside structure are around 3 kJ/mol higher using the UDFT geometry, but the TD-DFT geometries fail to provide meaningful SAPT0 values for inside structures. The DLPNO-CCSD(T) results support this conclusion: The description with TDDFT leads to around 5 kJ/mol higher energies for both isomers, indicating that UDFT provides a better description of the global minimum. Thus, for further analysis in the main manuscript as well as in the supporting information, the UDFT geometries are used.

Still, the question whether the up and down isomer differ significantly remains to be answered. Comparisons of the relative energies and frequencies obtained by UDFT as well as the relative energies obtained *via* SAPT0 and LED-DLPNO-CCSD(T) are shown in table S2. No method estimates a *ΔE* greater than 0.3 kJ/mol between the up and down conformation so that the in and out motifs can be interpreted as doubly-degenerated states with respect to the ring puckering. Both configurations exhibit nearly equal OH stretching frequencies, thus differentiating between both structures in the experimental spectrum is not possible.

Table S2: Comparison of energies and frequencies obtained by UDFT, SAPT0 and DLPNO-CCSD(T) for the up/down configurations of both inside and outside motif. The corresponding spin expectation value of the UDFT calculation does not show significant spin contamination.

Geo	Puckering	$\langle S^2 \rangle$	ΔE(UDFT)	$\tilde{\nu}$(OH) in cm^{-1}	ΔE(SAPT0) in kJ/mol	ΔE(DLPNO-CCSD(T)) in kJ/mol
in	up	2.025	0.15	3690	0	0.30
in	down	2.025	0	3693	0.02	0
out	up	2.024	0.02	3635	0.10	0.07
out	down	2.024	0	3632	0	0

A detailed discussion of the energy decomposition analysis obtained *via* SAPT0 can be found in the main manuscript, while a complete decomposition of the SAPT0 energy is given in table S3. To simplify discussion, only the slightly more stable down configuration is considered when analyzing the triplet states. The results of the LED-DLPNO-CCSD(T) method are discussed in the following.

Table S3: Results of energy decomposition analysis by SAPT0/jun-cc-pVDZ. The raw values for each interaction for the respective electronic state and isomer (col. 2-5), the energy difference between the *inside* and *outside* isomer for each interaction (col. 6,7) and the change in ΔE going from the S_0 to T_1 state (col. 8). A detailed explaination and derivation of all contributions can be found in literature.[5] The electrostatic and exchange contribution only consist of one term, the induction interaction consists of three terms $E_{ind,resp}^{(20)}$, $E_{exch-ind,resp}^{(20)}$, $\delta_{HF}^{(2)}$. The dispersion interaction is split into $E_{disp}^{(20)}$ and $E_{exch-disp}^{(20)}$, which can be seperated further into same-spin and opposite-spin parts. All values in kJ/mol.

	Inside (S0)	Outside (S0)	Inside (T1)	Outside (T1)	ΔE(S0)	ΔE(T1)	ΔΔE(S0,T1)
E_{elst}	-57.9	-60.4	-43.5	-50.8	2.5	7.3	4.8
$E_{elst}^{(10)}$	-57.9	-60.4	-43.5	-50.8	2.5	7.3	4.8
E_{exch}	57.5	58.7	50.4	56.5	-1.2	-6.1	-4.8
$E_{exch}^{(10)}$	57.5	58.7	50.4	56.5	-1.2	-6.1	-4.8
E_{ind}	-18.2	-18.9	-13.5	-16.0	0.6	2.4	1.8
$E_{ind,resp}^{(20)}$	-24.1	-27.0	-19.3	-24.0	2.9	4.7	1.8
$E_{exch-ind,resp}^{(20)}$	13.4	15.8	11.6	14.7	-2.4	-3.1	-0.6
$\delta_{HF}^{(2)}$	-7.5	-7.7	-5.9	-6.7	0.2	0.8	0.6
E_{disp}	-16.4	-15.2	-15.2	-14.0	-1.3	-1.2	0.0
$E_{disp}^{(20)}$	-20.0	-18.9	-18.2	-17.3	-1.1	-0.9	0.2
$E_{exch-disp}^{(20)}$	3.5	3.7	2.9	3.3	-0.2	-0.4	0.5
$E_{disp,SS}^{(20)}$	-10.0	-9.4			-0.5		
$E_{disp,OS}^{(20)}$	-10.0	-9.4			-0.5		
$E_{exch-disp,SS}^{(20)}$	2.0	2.1			-0.1		
$E_{exch-disp,OS}^{(20)}$	1.5	1.6			-0.1		
E_{tot}	-35.1	-35.7	-21.8	-24.2	0.6	2.4	1.8

Table S4: Energy decomposition analysis with LED-DLPNO-CCSD(T)/def2-TZVP, $\Delta E_{geo-prep}$ is the energetic penalty for distorting the monomers into the dimer geometry, $\Delta E_{el-prep}^{ref.}$ is the electronic preparation in the reference (Hartree-Fock), $E_{elstat}^{ref.}$ and $E_{exch}^{ref.}$ describe the electrostatic and exchange inter-fragment contributions in the reference (HF), while $E_{disp.}^{C-CCSD}$ describe the dispersive contribution from the correlation energy. $\Delta E_{non-disp.}^{C-CCSD}$ contains some electronic preparation from the correlation energy, but also any non-dispersive correlation energy (charge transfer, intrafragment double excitations and singles contributions). $\Delta E_{int}^{C-(T)}$ describes the change for the triples correction. Δ(S_0) and Δ(T_1) describe the difference between inside and outside isomer for each contribution, with positive values indicating a preference for the outside isomer. All values in kJ/mol.

	Inside (S_0)	Outside (S_0)	Inside (T_1)	Outside (T_1)	Δ(S_0)	Δ(T_1)
$\Delta E_{geo-prep}$ (Chromon)	0.6	0.3	0.2	-0.2	0.3	0.5
$\Delta E_{geo-prep}$ (MeOH)	0.1	0.2	0.2	0.5	-0.2	-0.3
$\Delta E_{el-prep}^{ref.}$ (Chromon)	92.5	95.9	72.5	81.9	-3.4	-9.3
$\Delta E_{el-prep}^{ref.}$ (MeOH)	82.0	81.8	70.8	77.4	0.3	-6.6
$E_{elstat}^{ref.}$	-166.1	-171.3	-135.1	-154.8	5.1	19.7
$E_{exch}^{ref.}$	-29.1	-29.1	-26.3	-28.1	0.0	1.9
$\Delta E_{non-disp.}^{C-CCSD}$	3.9	3.3	5.8	6.9	0.5	-1.1
$E_{disp.}^{C-CCSD}$	-13.7	-12.7	-14.0	-12.5	-1.1	-1.5
$\Delta E_{int}^{C-(T)}$	-2.0	-2.0	-1.5	-0.7	-0.1	-0.8
ΔE (total)	-31.9	-33.4	-27.4	-29.7	1.5	2.4

As discussed above and in the main manuscript, LED-DLPNO-CCSD(T) predicts the outside isomer as the more stable isomer both in the S_0 and T_1 state. Although SAPT0 and LED-DLPNO-CCSD(T) are difficult to compare directly due to their different approach (SAPT: pertubative, DLPNO: supramolecular), careful analysis is still possible. This shows *e.g.* that, similar to the SAPT0 values, the electrostatic interaction is the strongest attractive interaction with dispersion being significantly weaker. Comparing the contributions for the inside and outside isomer, nearly all contributions are equal in value except the attractive electrostatic interaction as well as the related electronic preparation of the chromone. This can be interpreted as better orbital overlap between the carbonyl group and the OH group of the methanol for the outside motif, resulting in a stronger hydrogen bond and overall higher binding energy in the S_0 state. Analyzing the T_1 state confirms the main theses in the main manuscript. The ΔE is mostly influenced by the electronic preparation of both MeOH and chromone as well as the electrostatic interaction. Although the electronic preparation penalty is higher for the outside isomer by 9.3 and 6.6 kJ/mol (15.9 kJ/mol total), this is more than compensated by the increased electrostatic contribution of 19.7 kJ/mol resp. to the inside isomer. We observe again a side dependence in the triplet state, resulting in significantly increased electronic preparation for the methanol, adapting to the flexible outside pocket. Furthermore, the binding energy is lowered upon electronic excitation, again coinciding with SAPT0 results. Finally, the negative geo-prep energy for the chromone molecule is of course unphysical. Since the deformation energy seems to be quite small (< 0.5 kJ/mol), this numeric error occurs due to the accuracy of the DLPNO-CCSD(T) method. Deformation energies calculated by DFT are discussed in the following, and confirm this hypothesis.

Binding and deformation energies

The OH stretching frequency of an H-donor is closely related to the strength of the hydrogen-bond established with the H-acceptor. Thus, the observed blue-shift of the OH stretching frequency switching from the S_0 to the T_1 state should be visible in binding energy calculations. The binding energy is calculated in following manner:

$$E_{BDE} = E'_{Chromon} + E'_{MeOH} - E_{Dimer}$$

$$with: E'_{Chromon}, E'_{MeOH} = Energy\ of\ resp.molecule\ in\ the\ dimer\ geometry$$

For the discussion of the BDE, we deliberately chose not to apply a BSSE correction. A comparing simulation for the S_0 geometries reveals that the difference between *"inside"* and *"outside"* is insignificant (both: 3.9 kJ/mol). Furthermore, it is known that the the usual counter-poise correction[6] scheme can lead to deviations from the true BDE[7]. Finally, the deformation energy is calculated in a similar manner by taking the energy difference of the relaxed monomer and the monomer in the dimer geometry.

Table S5: Binding and deformation energies for the chromone-MeOH cluster for the S_0 and T_1 state for both geometries (inside/outside). For the triplet state, the puckering of the 4-pyrone ring is also considered. All values are given in kJ/mol.

State	Geo	Puckering	Method	BDE	E_{Def}(Chromon)	E_{Def}(MeOH)
S_0	in	-	DFT	40.2	0.8	0.5
S_0	out	-	DFT	41.2	0.5	0.6
T_1	in	up	UDFT	35.5	0.6	0.3
T_1	in	down	UDFT	35.6	0.6	0.4
T_1	out	up	UDFT	38.6	0.2	0.4
T_1	out	down	UDFT	38.6	0.2	0.4

Starting with the deformation energies, it is remarkable how all values are below 1 kJ/mol, indicating low barriers for reorganization. The binding energy is strongest for the outside isomer in general, which is reasonable, since it is the global minimum. The observed blue-shift of the OH stretching frequency can be explained by the reduced binding energy in the triplet state, while the larger splitting of the frequencies of the two relevant isomers is caused by the increased difference in binding energy from 1 kJ/mol to 3 kJ/mol.

Barriers for isomer interconversion

As explained in the main manuscript, the interconversion barriers between different isomers were calculated by relaxed scans along an appropriate coordinate with the results shown below (fig. S18-22).

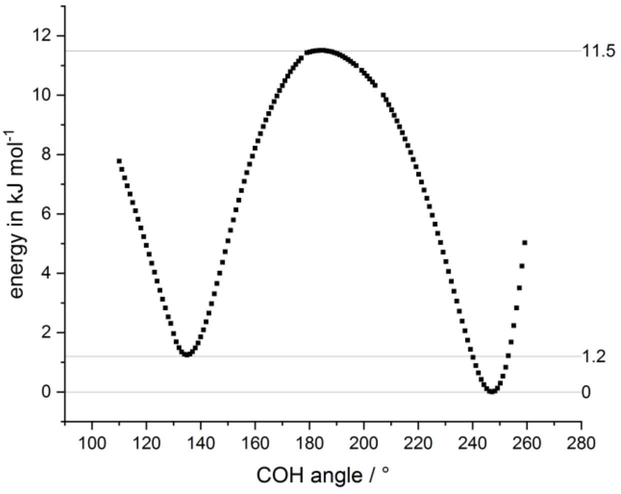

Figure S18: Interconversion barrier between inside and outside isomer in the S0 state

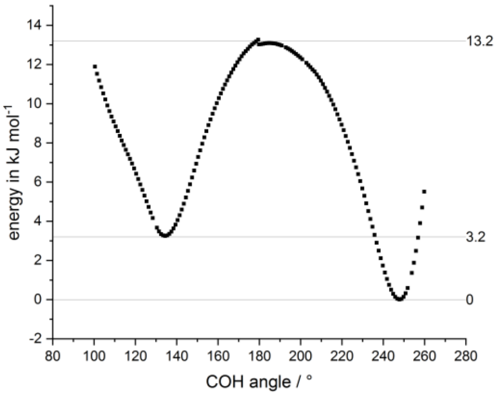

Figure S19: Interconversion barrier between inside and outside isomer in the T1 state (down configuration)

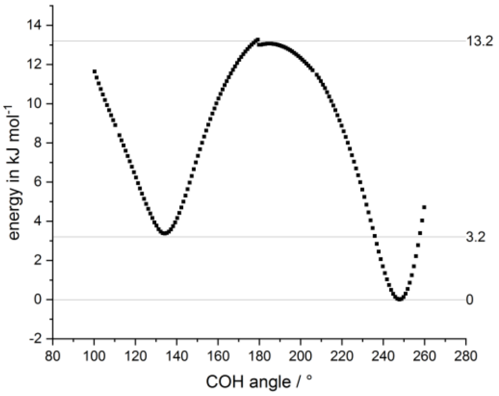

Figure S20: Interconversion barrier between inside and outside isomer in the T1 state (up configuration).

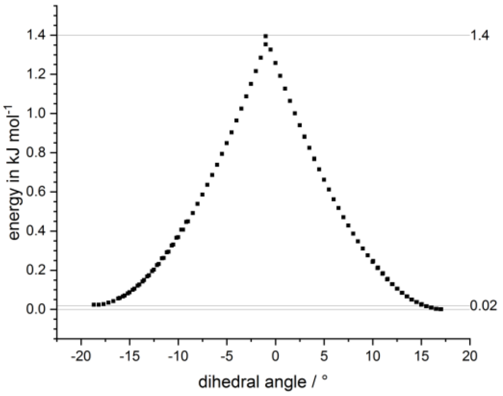

Figure S21: Interconversion barrier between up and down isomer in the T1 state (outside motif), the lowest line denotes the zero (omitted for clarity).

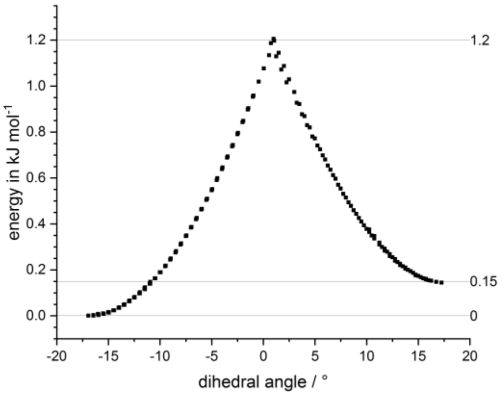

Figure S22: Interconversion barrier between up and down isomer in the T1 state (inside motif)

References

1 T. Itoh, *J. Photochem. Photobiol. A: Chem.*, 2010, **214**, 10–15.

2 K. Bartl, A. Funk and M. Gerhards, *ChemPhysChem*, 2009, **10**, 1882–1886.

3 R. L. Martin, *J. Chem. Phys.*, 2003, **118**, 4775–4777.

4 M. Baba, *J. Phys. Chem. A*, 2011, **115**, 9514–9519.

5 B. Jeziorski, R. Moszynski and K. Szalewicz, *Chem. Rev.*, 1994, **94**, 1887–1930.

6 S. F. Boys and F. Bernardi, *Mol. Phys.*, 2006, **19**, 553–566.

7 a) J. R. Alvarez-Idaboy and A. Galano, *Theor. Chem. Acc.*, 2010, **126**, 75–85; b) A. Galano and J. R. Alvarez-Idaboy, *J. Comput. Chem.*, 2006, **27**, 1203–1210; c) J. C. López, J. L. Alonso, F. J. Lorenzo, V. M. Rayón and J. A. Sordo, *J. Chem. Phys.*, 1999, **111**, 6363–6374; d) H. Valdés and J. A. Sordo, *J. Comput. Chem.*, 2002, **23**, 444–455; e) H. Valdés and J. A. Sordo, *J. Phys. Chem. A*, 2002, **106**, 3690–3701;